

In-Situ Monitoring of Phase Transition and Microstructure Evolution in Ni-Based Superalloys by Electrical Resistivity

Utada, Satoshi; Sasaki, Ryo; Reed, Roger C.; Tang, Yuanbo T.

DOI:

[10.1007/s11661-022-06924-7](https://doi.org/10.1007/s11661-022-06924-7)

License:

Creative Commons: Attribution (CC BY)

Document Version

Publisher's PDF, also known as Version of record

Citation for published version (Harvard):

Utada, S, Sasaki, R, Reed, RC & Tang, YT 2023, 'In-Situ Monitoring of Phase Transition and Microstructure Evolution in Ni-Based Superalloys by Electrical Resistivity: Direct Comparison With Differential Scanning Calorimetry and Application to Case Studies', *Metallurgical and Materials Transactions A*, vol. 54, pp. 1549–1567 . <https://doi.org/10.1007/s11661-022-06924-7>

[Link to publication on Research at Birmingham portal](#)

General rights

Unless a licence is specified above, all rights (including copyright and moral rights) in this document are retained by the authors and/or the copyright holders. The express permission of the copyright holder must be obtained for any use of this material other than for purposes permitted by law.

- Users may freely distribute the URL that is used to identify this publication.
- Users may download and/or print one copy of the publication from the University of Birmingham research portal for the purpose of private study or non-commercial research.
- User may use extracts from the document in line with the concept of 'fair dealing' under the Copyright, Designs and Patents Act 1988 (?)
- Users may not further distribute the material nor use it for the purposes of commercial gain.

Where a licence is displayed above, please note the terms and conditions of the licence govern your use of this document.

When citing, please reference the published version.

Take down policy

While the University of Birmingham exercises care and attention in making items available there are rare occasions when an item has been uploaded in error or has been deemed to be commercially or otherwise sensitive.

If you believe that this is the case for this document, please contact UBIRA@lists.bham.ac.uk providing details and we will remove access to the work immediately and investigate.



In-Situ Monitoring of Phase Transition and Microstructure Evolution in Ni-Based Superalloys by Electrical Resistivity: Direct Comparison With Differential Scanning Calorimetry and Application to Case Studies

SATOSHI UTADA, RYO SASAKI, ROGER C. REED, and YUANBO T. TANG

In this study, resistivity measurements are made during continuous heating and cooling on four different Ni-based superalloys of different grain structures and with different phases (*i.e.*, γ' and carbide). The results are directly compared with differential scanning calorimetry (DSC) profiles to identify the material's resistivity response. The resistivity measurements have been performed using an electro-thermal mechanical testing (ETMT) system having a capability of heating and cooling a sample at a rate of up to 100 K/s by Joule heating, which is not possible with standard heating methods used in previous *in-situ* microstructure analysis approaches. By comparing different precipitate variations and thermal histories, γ' volume fraction and precipitate number density are found to be the most important factors determining the resistivity of the materials. *In-situ* resistivity measurement was applied to several case studies to show that it can provide microstructural information in complex high temperature experiments.

<https://doi.org/10.1007/s11661-022-06924-7>
© The Author(s) 2022

I. INTRODUCTION

NI-BASED superalloys offer mechanical and environmental durability for high temperature applications such as the hot section of aero engines, power generating gas turbines, and turbochargers.^[1,2] Heat treatment is an essential part of manufacturing of Ni-based superalloys due to the large number of alloying elements that confer superior properties.^[1,3,4] While some applications do not require heat treatment and the material is used as-cast, multi-step heat treatments are usually applied as this microstructural optimization gives substantial improvement in mechanical properties. Thus, solvus and liquidus temperatures must be defined in order to solutionize and homogenize the γ/γ' system superalloys

during solution heat treatment, or to apply a subsolvus heat treatment depending on applications. The kinetics of γ' precipitation and growth are also of interest for adjusting precipitate size during aging treatments. Traditionally, thermal analyses such as differential thermal analysis (DTA) and differential scanning calorimetry (DSC) are used as the first step to determine heat treatment conditions.^[5–9]

In-situ measurement techniques such as neutron and synchrotron X-ray diffractometry are also utilized in order to understand microstructure evolution and phase transitions during continuous heating/cooling, γ' volume fraction and γ/γ' lattice misfit at different temperatures, and microstructural change during deformation of Ni-based superalloys.^[10–17] These are very powerful methods and they have provided substantial contributions to understanding in this research field. The most significant point detracting from these methods is the relatively limited access to these experimental facilities and their operating costs.

Electrical resistivity measurement is an *in-situ* method that can detect microstructural changes at various temperatures. It has been used to assess material properties in different metallic systems such as Al, Ti, and Zr alloys.^[18–21] In the case of Ni-based superalloys, it can be used to characterize grain growth,^[22] volume fraction of the γ' phase,^[23,24] and dissolution and precipitation kinetics of γ' phase.^[24,25] However,

SATOSHI UTADA and YUANBO T. TANG are with the Department of Materials, University of Oxford, Parks Road, Oxford, OX1 3PH, UK. Contact e-mail: satoshi.utada@materials.ox.ac.uk RYO SASAKI is with the Metallurgical Research Laboratory, Hitachi Metals, 1240-2 Hashima-cho, Yasugi, Shimane, 692-0014, Japan. ROGER C. REED is with the Department of Materials, University of Oxford and also with the Department of Engineering Science, University of Oxford, Parks Road, Oxford, OX1 3PJ, UK.

Manuscript submitted July 31, 2022; accepted November 25, 2022.

Article published online December 28, 2022

Table I. Chemical Composition of Experimental Alloys in Wt pct (Ni Bal.)

Alloy	Co	Cr	Mo	W	Ta	Fe	Al	Ti	Nb	Re	Hf	Si	C	B	Zr
Waspaloy	12.33	19.5	3.81			1.44	1.33	3.02					0.04	0.005	0.05
AD730®	8.88	16.19	3.14	2.79		4.2	2.44	3.64	1.12				0.01	0.011	0.032
STAL15	5.24	15.06	0.97	3.83	8.21	0.03	4.44		0.01		0.95	0.18	0.035		
CMSX-4®	9.74	6.25	0.62	6.59	6.95	0.03	5.88	0.99		3.31	0.087				

electrical current can accelerate recovery and recrystallization, and it can, in principle, affect the phase transformation process in metallic materials.^[26–28] Several studies have made attempts to extract microstructural information from Ni-based superalloys through electrical resistivity measurement.^[22,23,25,29–33] Other studies directly compared DSC and resistivity for analyses of physical properties, but data on superalloys are particularly limited.^[19–21,34,35] Overall, the analyses so far have been limited to specific and fundamental uses, and there is a need for comprehensive understanding to make the best use of this method.

In this study, the resistivity of four different Ni-based superalloys was measured during continuous heating and cooling using an electro-thermal mechanical testing (ETMT) system that uses the Joule effect for controlling specimen temperature.^[23,36] Results are compared with the standard DSC method to rationalize the resistivity response caused by the microstructural changes in the materials. Different heating and cooling rates were used in order to understand factors that can affect the resistivity of the materials. In this way, it is shown that measurement and analysis of resistivity changes helps to understand a material's state in a non-destructive way.^[34] Finally, three different case specific experiments that take advantage of *in-situ* resistivity measurement are presented and discussed to illustrate how the results can be used to interpret microstructural evolution.

II. EXPERIMENTAL METHODS

A. Materials

A total of four different Ni-based superalloys, Waspaloy, AD730® (AD730 is a registered trademark of Aubert & Duval), STAL15 and CMSX-4® (CMSX-4 is a registered trademark of Cannon-Muskegon) were characterized in this study. The analyzed compositions of the materials are in Table I, their processing histories are given in Table II, and their initial microstructures are shown in Figure 1. Waspaloy is an age-hardened superalloy produced by the cast and wrought process and it is one of the most widely used alloys for turbine disc and ring seal applications in gas turbines.^[37,38] Waspaloy bars were received in the as heat-treated state. AD730® is a cast and wrought alloy having superior high temperature performance compared to Waspaloy, nevertheless, with good hot workability.^[39,40] AD730® was received in the form of as-forged billet. STAL15 is single crystal (SX) superalloy designed for industrial gas turbine application with very good resistance to

environmental degradation and contains carbon for casting defect tolerance.^[41,42] CMSX-4® is another SX superalloy with balanced high temperature mechanical properties and hence is one of the most popular Ni-based SX superalloy used for turbine blades of aero engines.^[43] The two types of SX superalloys were received as fully heat-treated bars. In addition to the Ni-based superalloys above, commercially pure Ni (purity 99.45 pct) was also used in this study.

B. In-situ Resistivity Measurement Using Electro-Thermal Mechanical Testing (ETMT) System

Figure 2 illustrates the setup of the ETMT system for measuring resistivity during heating and cooling. Specimens were extracted from the bars or billet using electric discharge machining (EDM) into the geometry shown in Figure 2(a). This $1 \times 1 \text{ mm}^2$ cross section was chosen to minimize temperature variation from the core to the surface of the specimen.^[28,44] Four sides of the specimen gauge were polished to P4000 grade SiC abrasive paper to remove the surface layer affected by EDM. Either a R-type thermocouple or a K-type plus R-type dual thermocouples were used for controlling the temperature. The R-type thermocouple has a $\pm 10 \text{ K}$ error at 1100°C due to its sensitivity to thermal-electric voltage that can be disrupted by electrical current that cannot be avoided in the Joule heating method (parasitic voltage effect).^[45] Because of the high electrical current density (especially at temperatures above 1200°C), thermal electric voltage can be influenced easily, and this may cause an inaccurate temperature reading up to $\pm 25 \text{ K}$. Additionally, two Pt (99.99 pct) wires were used to measure the electrical potential difference instead of alumel (Ni–2Al–2Mn–1Si) wires used in the previous study.^[34] Because all the tests were performed in air, Pt wires were chosen for better oxidation resistance and durability at very high temperature above 1200°C . All wires used in this study have 0.125 mm diameter and were supplied by Goodfellow as qualified thermocouple wires. The tips of thermocouples were made into a 0.5 mm diameter bead by inert gas arc welding. Thermocouple beads were spot-welded at the gauge center and the two Pt wires were spot-welded 1.5 mm away from each side of the thermocouples. This 3 mm center part between two Pt wires was considered as gauge section for tensile straining and resistivity measurement. Specimen thickness and width were measured by a micrometer prior to the experiments. Figure 2(b) shows a sample after attaching all wires. Configuration of the ETMT system with a miniature

Table II. Processing History of Experimental Alloys

Alloy	Type	Received State	Heat Treatments	Remarks
Waspaloy	cast and wrought	16.4 mm diameter bar heat-treated	1010 °C/4 h/water quench → 843 °C/4 h/air quench (AQ) → 760 °C/16 h/AQ	
AD730®	cast and wrought	10 inch billet as-forged		ETMT samples were taken from 30 mm away from outer diameter
STAL15	investment single crystalline casting (bridgman casting)	25 mm diameter bar heat-treated	1300 °C/5 h/AQ → 1100 °C/6 h/AQ → 850 °C/20 h/AQ	crystallographic misorientation < 5 deg from ⟨001⟩
CMSX-4®	investment single crystalline casting (bridgman casting)	14 mm diameter bar heat-treated	1321 °C/2 h/AQ → 1140 °C/6 h/AQ → 870 °C/20 h/AQ	crystallographic misorientation < 5 deg from ⟨001⟩

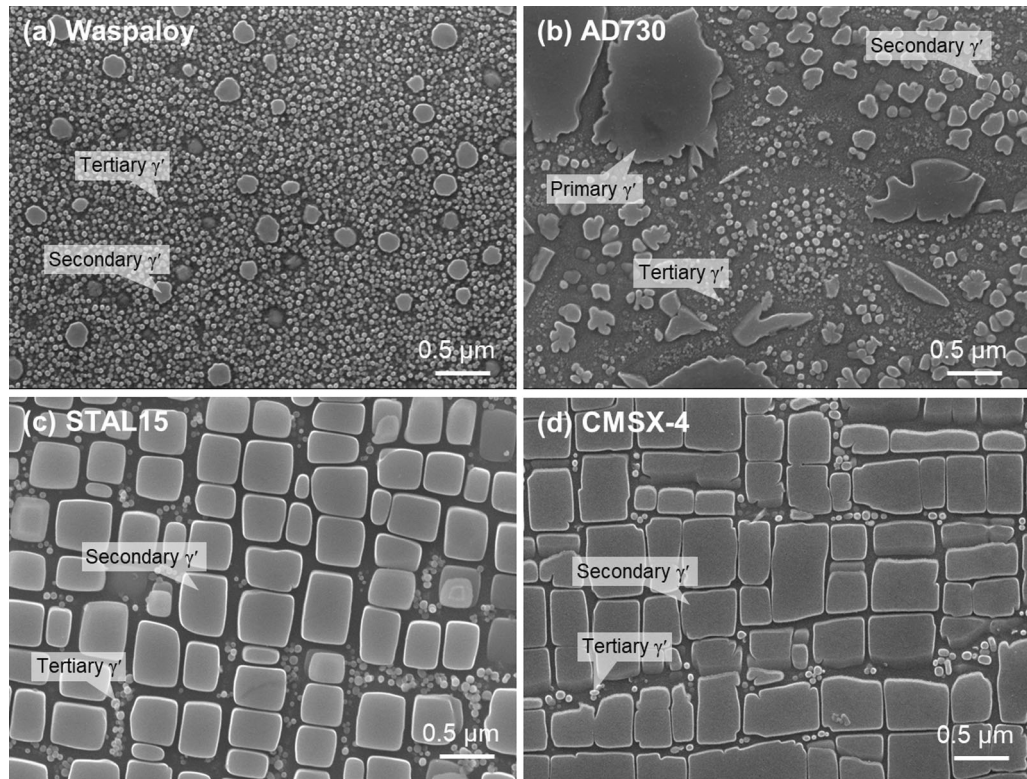


Fig. 1—Initial microstructure of experimental superalloys used in this study. (a) Waspaloy, (b) AD730®, (c) STAL15, (d) CMSX-4®.

specimen held by water-cooled grips is shown in Figure 2(c).

Before heating for the resistivity measurements, each specimen's temperature distribution was checked using a FLIR 655sc infrared (IR) thermal camera equipped with T198059 close-up IR lens having a spatial resolution of 50 μm . Specimen surfaces were coated with LabIR® HERP-HT-MWIR-BK-11 thermographic spray paint to achieve a high emissivity surface. The specimen position was carefully set to ensure the highest temperature of the parabolic temperature distribution across axial direction^[46] is located at the spot-welded thermocouple.

Whilst the thickness and width of the resistivity measurement section has been measured by a micrometer, the length of the measured section is fixed at 3 mm. However, during heating, the material will experience thermal expansion; the thermal expansion coefficient of Ni-based alloys is in the range of 1.3 to $1.7 \times 10^{-5}/^\circ\text{C}$. Because the thermal expansion is not linear, measurement is needed for accuracy especially for detection of phase transition temperatures. The thermal strain was measured by digital image correlation (DIC) using an iMetrum non-contact video extensometry system with VideoGauge software, which was used in previous

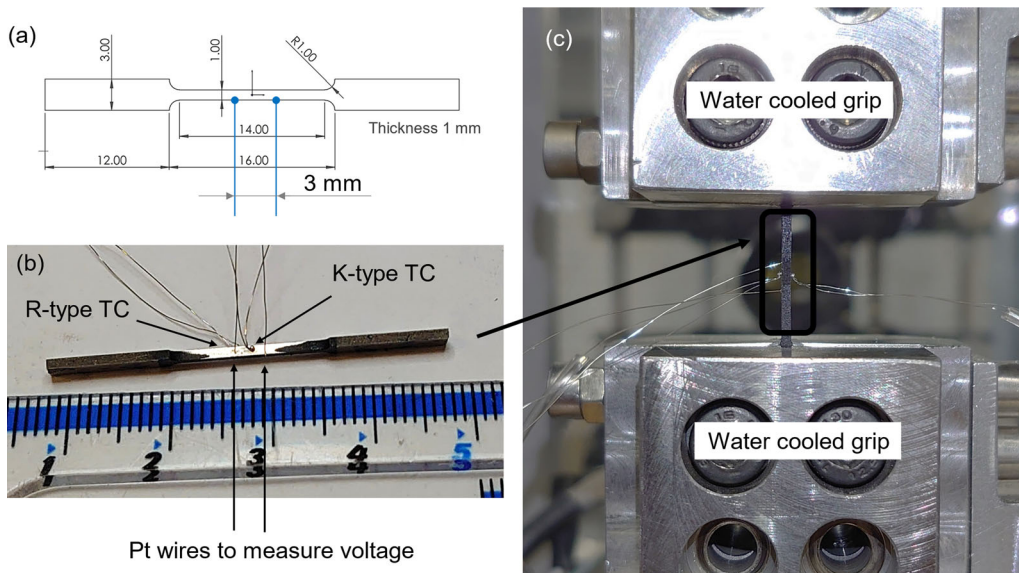


Fig. 2—Experimental setup of resistivity measurement using miniature testing specimen and the ETMT system. (a) geometry of a specimen having 1 mm × 1 mm section. (b) Miniature specimen after spot welding K-type thermocouple (TC), R-type TC, and Pt wires for measuring electrical potential difference. (c) Miniature specimen held by water cooled grips at both ends.

studies.^[34,46] VHT flame proof high temperature spray paint was used to apply speckle patterns on the sample surface to track the thermal strain. This video extensometry setup can measure the specimen's strain up to 1100 °C due to the temperature capability of the paint and incandescence.

Experimentally measured thermal strains of AD730® and CMSX-4® are shown in Figure 3. They show reasonably good agreement with the results from CMSX-4® obtained using dilatometry by Epishin *et al.*^[47] Thermal strain ε_T above 1100 °C was extrapolated using curve fitting Eq. [1] from the study by Epishin *et al.*^[47]

$$\varepsilon_T(T) = a + bT + ce^{dT} \quad [1]$$

Fitting parameters obtained for the present study are $a = -9.049 \times 10^{-4}$, $b = 1.524 \times 10^{-5}/^\circ\text{C}$, $c = 6.384 \times 10^{-6}$, and $d = 5.77 \times 10^{-3}/^\circ\text{C}$, and T is the temperature of the material in °C. The same fitting equation using temperature in K gives an almost identical fitting parameter for b . The fitting parameter b is in the same order as the thermal expansion coefficient of Ni-base alloys (1.3 to $1.7 \times 10^{-5}/^\circ\text{C}$) which validates that this fitting is practical. Resistivity was then obtained by applying Eq. [1] for calculating the thermal expansion of the measurement volume at the temperature of measurement.

Tensile plastic straining was also performed on STAL15 and CMSX-4®. Samples were heated in the ETMT system (equipped with a 5 kN load cell) by Joule heating, and the same video extensometry system with DIC was used for strain measurement within a 3 mm of gauge center consistent with our other studies.^[36,46] Deformation rate was controlled by a displacement

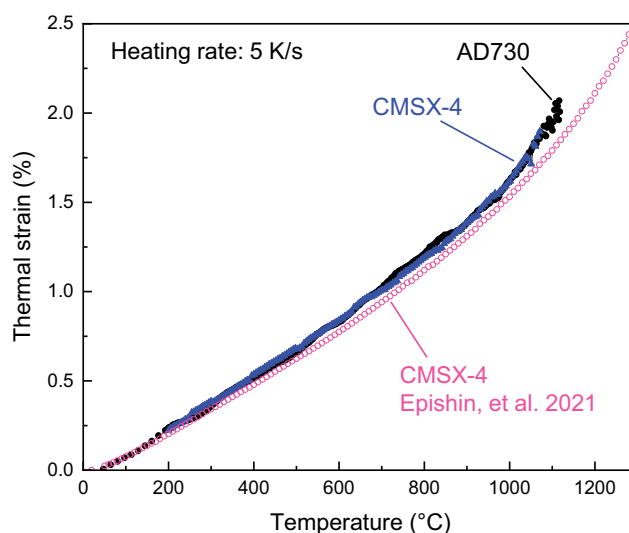


Fig. 3—Thermal strain of AD730® and CMSX-4® measured by video extensometry during heating in the ETMT at 5 K/s. Result from the study by Epishin *et al.*^[47] is also plotted for comparison.

measured by a linear variable displacement transducer (LVDT).

C. Differential Scanning Calorimetry (DSC)

DSC was conducted using a Netzsch DSC 404 F1 Pegasus (heat flux type DSC) having temperature and sensitivity calibrated using 6 pure metals (In, Bi, Zn, Sn, Al, Au) as references. Superalloy samples were polished to P2500 grit SiC abrasive paper to have a 60 to 70 mg mass and they were placed inside a PtRh crucible/lid with an Al₂O₃ liner in a PtRh chamber. Heating and cooling rates were 10 K/min (0.17 K/s) under an argon

atmosphere. The baseline was measured using an empty crucible and the same heating/cooling cycle prior to measurements on superalloy samples. In addition, phase equilibria were calculated using ThermoCalc software and the TTNi8 database for all four alloys. Calculated values were used to aid in the identification of phase transition temperatures following DSC and resistivity measurements.

D. Microstructure Characterization

Specimens after thermal and mechanical experiments were polished up to 1 μm diamond suspension and finished by colloidal silica suspension for

microstructural characterization. Three different field emission gun scanning electron microscopes (FEG-SEM) were used for different techniques. Electrolytic etching was employed using 15 pct phosphoric acid at 3 V to expose γ' precipitates and a JEOL JSM-6500F was used to obtain secondary electron images (SEI) of the γ/γ' microstructure. Electron channeling contrast images (ECCI) were obtained using a Zeiss Crossbeam 540 FEG-SEM with Gemini 2 column. ECCI images were acquired at an accelerating voltage of 30 kV and probe current 5 nA with a stage tilt of 10 deg. A Zeiss Merlin FEG-SEM with Gemini 2 column and a Bruker electron backscatter diffraction (EBSD) system was used for confirming that recrystallization had taken place in one of the case study experiments explained in a subsequent section.

III. FUNDAMENTAL RESULTS ON RESISTIVITY MEASUREMENTS

A. General Resistivity Response During the Heating and Deformation of Ni-Based Materials

The resistivity of metallic materials generally increases monotonically with increasing temperature due to phonon vibration as observed for commercially pure Ni shown in Figure 4.^[23,48] Two heating and cooling rate experiments were performed on pure Ni at 5 and 0.33 K/s (20 K/min). For both rates, curves were overlapping during all period and showed a kink at 323 $^{\circ}\text{C}$, which represents the Curie temperature of this material. Because the purity of this Ni sample was not particularly high (99.45 pct), the Curie temperature is slightly lower than the theoretical one of 354 $^{\circ}\text{C}$. The resistivity variation above the Curie temperature revealed linear behavior with increasing temperature.

Figure 5 shows various measurements that can be done by the ETMT system. Resistivity of superalloys

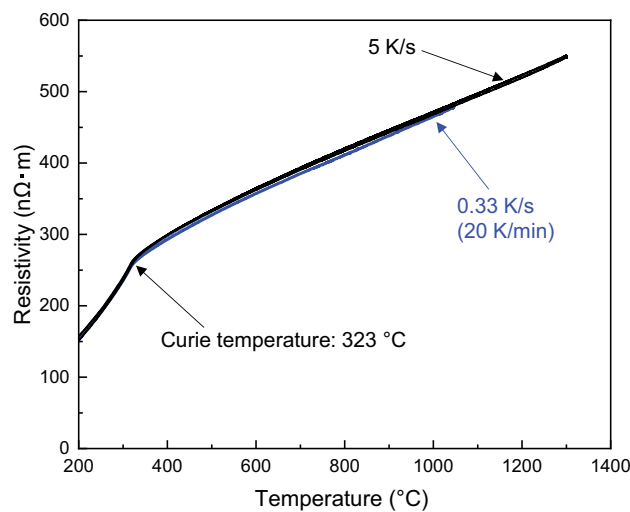
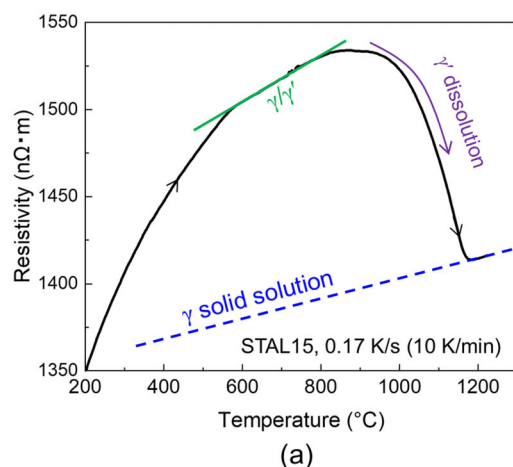
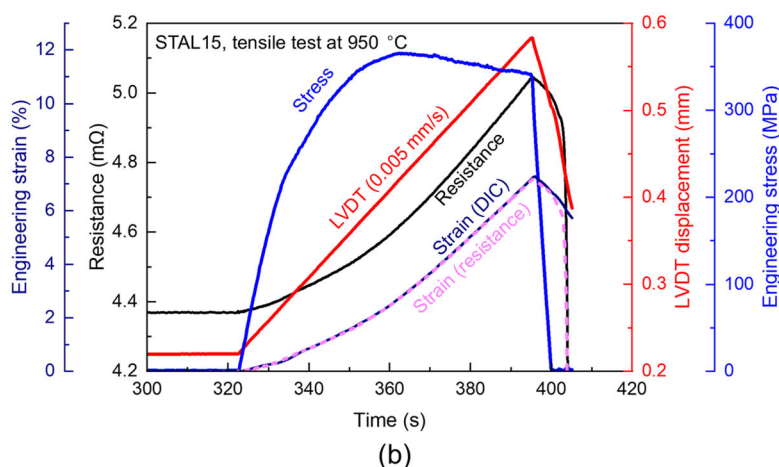


Fig. 4—Resistivity of commercially pure Ni measured during two different heating/cooling rates, 5 and 0.33 K/s (20 K/min). Temperature was measured by a K-type thermocouple up to 400 $^{\circ}\text{C}$ and by an R-type thermocouple above 400 $^{\circ}\text{C}$.



(a)



(b)

Fig. 5—(a) Resistivity of STAL15 during heating at 0.17 K/s. Temperature was measured by R-type thermocouple. (b) Tensile test on STAL15 at 950 $^{\circ}\text{C}$ with strain rate $1.7 \times 10^{-3} \text{ s}^{-1}$ (plastic regime) up to 6 pct plastic strain. Electrical resistance (black), displacement by LVDT (red), engineering strain by DIC (violet), engineering strain by resistance (cyan) and engineering stress (blue) are presented as a function of time (Color figure online).

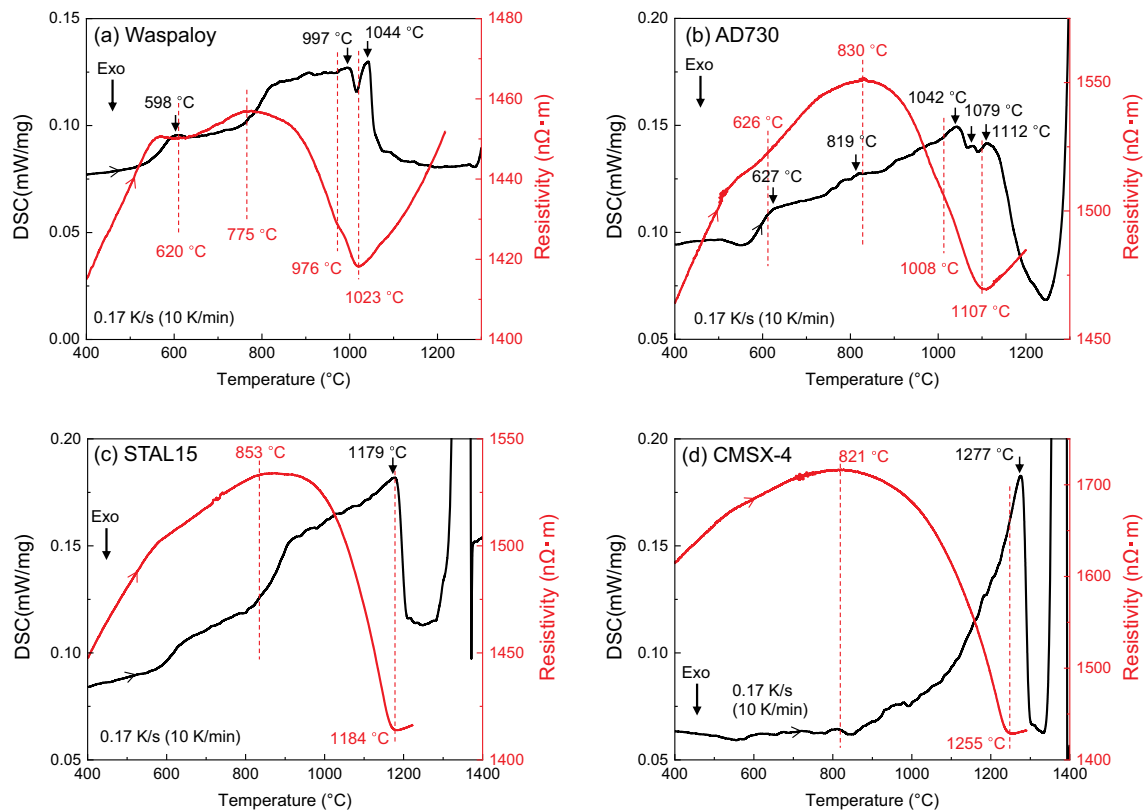


Fig. 6—DSC profile (black curve) and resistivity (red curve) of Waspaloy (a), AD730® (b), STAL15 (c), and CMSX-4® (d), at heating rate of 0.17 K/s (10 K/min) as a function of temperature. Temperature was measured by R-type thermocouple (Color figure online).

during continuous heating typically presents three different sections, as is shown in Figure 5(a) which is demonstrated on STAL15 Ni-based SX superalloy at a heating rate of 0.17 K/s: increasing resistivity with constant γ/γ' phase microstructure, decreasing resistivity due to γ' dissolution, and linear increasing resistivity of γ phase solid solution. Different STAL15 sample was deformed in tension at 950 °C with a strain rate of 10^{-3} /s up to 6 to 7 pct plastic strain as shown in Figure 5(b). LVDT displacement is the controlling mode that has linear increment during the test. Both electrical resistance and engineering strain shows linear increments in the plastic regime, whereas the elastic regime is not having constant deformation rate due to intrinsic temperature distribution effect of high temperature tests in the ETMT system.^[45] The strain measured by DIC^[46] and strain calculated from the electrical resistance^[36] are overlapping that giving identical values to each other. Because extension of electrical potential measuring section affects electrical resistance heavily, microstructural change during the deformation could not be detected by the resistivity. This STAL15 sample after interrupted tensile test was then used for one of the case studies in later section.

B. Direct Comparison of DSC and Resistivity for Detecting Phase Transition

The heating thermograms of DSC analysis on four different superalloys are shown in Figure 6 with resistivity profiles at the same heating rate, 0.17 K/s (10 K/min). Arrows are pointing at different peaks and inflections of curves to indicate phase transitions. Peaks and inflections were identified using the first derivative of curves. Waspaloy and AD730® exhibit multiple peaks in the DSC profile before complete γ' dissolution. STAL15 and CMSX-4® have a more pronounced γ' dissolution due to a higher γ' volume fraction and less variety of precipitate types. A summary of phase transitions detected by DSC and resistivity measurements is given in Table III.

In the heating of Waspaloy in the DSC (Figure 6(a)), the endothermic peak at 1044 °C is the γ' solvus including intergranular precipitates.^[49] The peak before the γ' solvus at 997 °C is consistent with the dissolution of $M_{23}C_6$ carbide phase.^[49] This behavior during heating is reflected in the resistivity curve which has multiple inflections. The decreasing resistivity at 775 °C indicates the onset of γ' phase dissolution. During γ' phase

Table III. Summary of Phase Transition Temperatures (°C) Obtained by ThermoCalc TTNi8 Database (Calculated Equilibrium), DSC (Heating Rate 0.17 K/s) and Resistivity (Heating Rate 0.17 K/s)

Alloy	Method	Liquidus	Solidus	MC	γ'	Onset of γ' Dissolution	$M_{23}B_2$	$M_{23}C_6$	P/σ	μ
Waspaloy	TTNi8	1364	1266	1304	1022			964		664
	DSC	1396	1287	—	1044	760		997		
AD730®	resistivity				1023	775		976		
	TTNi8	1347	1258	1275	1113		1079	953	847	698
	DSC 1st	1345	1247	1325	1112	765	1080		819	
STAL15	resistivity				1107	830		1008		
	TTNi8	1357	1296	1324	1152			1030		
	DSC 1st	1361	1302	1350	1179	800				
CMSX-4®	resistivity				1184	853				
	TTNi8	1373	1307		1268				1212	
	DSC 1st	1385	1335		1277	840				
	resistivity				1255	821				

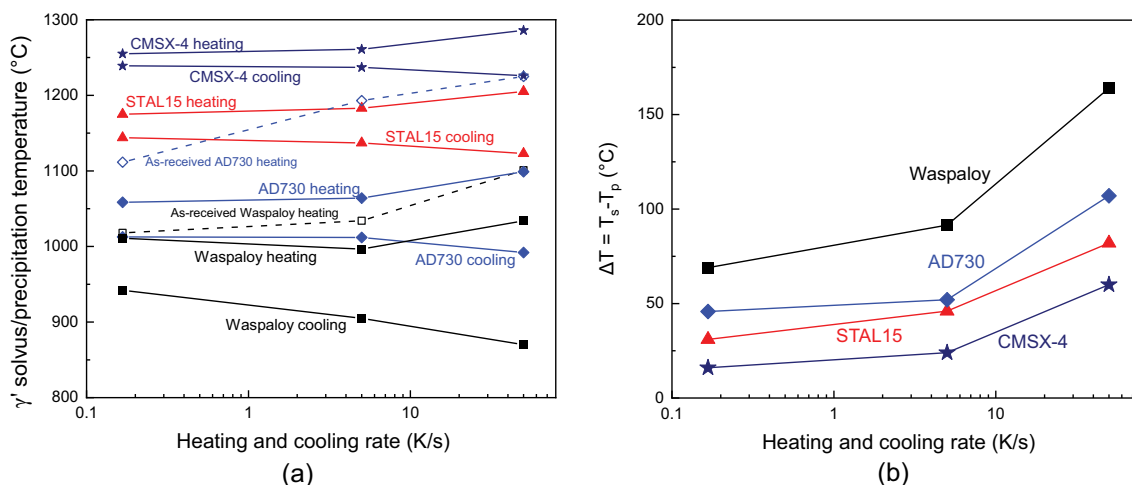


Fig. 7—(a) γ' solvus and re-precipitation temperatures of four superalloys after cooled at 5 K/s from supersolvus temperatures (solid lines) and as-received state (dashed lines) defined by resistivity. (b) Difference between T_s (γ' solvus) and T_p (γ' precipitation) defined by resistivity as a function of heating and cooling rates.

dissolution, there is a small transition at 976 °C, which probably corresponds to $M_{23}C_6$ carbide dissolution. This carbide dissolution is in good agreement with the previous study reporting grain boundary cavitation after overheating at 1000 °C.^[34]

Like Waspaloy, AD730® (Figure 6(b)) also has DSC peaks corresponding to dissolution of $M_{23}C_6$ and γ' phases at 1042 °C and 1112 °C, respectively. The solvus temperature of $M_{23}C_6$ was identified as a small kink during decreasing resistivity at 1008 °C and that of γ' is the peak shown at 1107 °C in the resistivity curve. Minor $M_{23}B_2$ boride is known to precipitate in AD730®,^[50] and its solvus was found in the DSC data with a small peak between those of $M_{23}C_6$ and γ' at 1079 °C, while it was difficult to distinguish in resistivity.

Waspaloy and AD730® have another common behavior of the resistivity curve inflection between 600 °C and 650 °C (Figures 6(a) and (b)). For example, Waspaloy has the DSC peak at 598 °C and dip between two upward resistivity peaks at 620 °C. AD730® has the resistivity curve inflection at 626 °C that matches with the DSC peak at 627 °C. These

seem to indicate a microstructural event potentially caused by dissolution or coalescence of very fine γ' precipitates with diameter less than 50 nm according to other studies.^[24,50] ThermoCalc TTNi8 database predicts a μ phase transition at 664 °C for Waspaloy, however, this is unlikely to occur since carbides are only possible minor phase in Waspaloy unless it is aged for more than 2000 hours.^[51]

SX superalloys, STAL15 (Figure 6(c)) and CMSX-4® (Figure 6(d)), have less complicated DSC thermograms and resistivity profiles compared to those of the polycrystalline (PX) superalloys. The γ' solvus temperatures were clearly identified for both STAL15 and CMSX-4® in the two different methods. ThermoCalc predicted the dissolution of P/μ phases at below 1212 °C for CMSX-4®; however, it is unlikely to be observed during heating at rate of 0.17 K/s. In fact, neither a peak nor a transition in the curve was found in both DSC and resistivity. Generally, 2nd generation SX superalloys have good enough γ/γ' stability to avoid the formation of such topologically close-packed (TCP) phases for at least 10 hours at 1000 °C.^[52,53]

Table IV. Heating and Cooling Cycles Applied to Waspaloy

Cycle	Heating/Cooling Rate	Purpose	Figures
(i)	5 K/s	microstructure reset	Figures 8, 10, 11(a), black
(ii)	5 K/s	benchmark	Figures 8, 10, red
(iii)	50 K/s	compare with 5 K/s (2) and 10 K/min (5) after 5 K/s	Figure 11(b), black
(iv)	5 K/s	compare with 5 K/s after 5 K/s (2)	Figure 11(b), red
(v)	10 K/min	compare with 5 K/s (2) and 50 K/s (3) after 5 K/s	Figures 8, 10, blue
(vi)	50 K/s	compare with 50 K/s after 5 K/s (3)	Figure 11(b), blue

The resistivity of the four alloys were measured using different heating and cooling rates (0.17, 5, 50 K/s) to compare the kinetics of γ' dissolution and re-precipitation. Solvus and re-precipitation temperatures were measured after cooling from supersolvus temperature at 5 K/s in the ETMT system. In addition, those for Waspaloy and AD730® were also obtained from as-received material. Solvus and re-precipitation temperatures are plotted in Figure 7(a) and the difference of solvus and re-precipitation temperatures is plotted in Figure 7(b). The results show typical behavior of delayed dissolution for faster heating rates and larger magnitudes of undercooling for faster cooling rates. Both Waspaloy and AD730® reveal a higher γ' solvus in as-received state compared to that after cooling at 5 K/s. Particularly at the fastest heating rate 50 K/s, complete dissolution of the γ' phase in AD730® occurred at a higher temperature than the γ' solvus of STAL15. Most probably, a very large primary γ' in Figure 1(b) is the reason for delaying complete dissolution in AD730®. Alloys with a lower γ' solvus (Waspaloy, AD730®) have large differences in solvus and re-precipitation temperature compared to SX superalloys (STAL15 and CMSX-4®) with higher solvus temperatures. The smallest difference for CMSX-4® is likely to be due to a faster diffusion at very high temperature that eases dissolution and re-precipitation.

C. Relationship Between Initial Microstructure and Heating Rate in Waspaloy

General resistivity responses are described in the previous subsection with a heating rate of 0.17 K/s (10 K/min). This section explains details of microstructure and resistivity behaviors during different heating and cooling rates which were studied for Waspaloy. Multiple heating and cooling cycles can create an irreversible effect on the microstructure and resistivity of a material.^[31] In this study, we confirmed that repeated heating and cooling cycles at 5 K/s created a reversible microstructure for Waspaloy (*i.e.*, repeated cycles of 5 K/s give identical resistivity profiles) which will be explained later in this section. Therefore, 5 K/s was determined to be a benchmark and used prior to different heating rates to compare the effect of different heating and cooling rates.

Six cycles of heating and cooling were performed on the same Waspaloy sample (cycles are listed in Table IV) without detaching any wires and without removing the sample from the ETMT machine to keep measurements

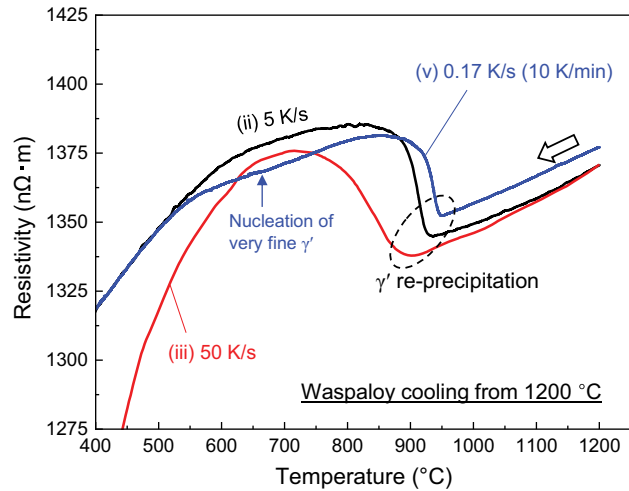


Fig. 8—Resistivity of Waspaloy during cooling down from 1200 °C at different cooling rates, 50, 5, and 0.17 K/s. Temperature was measured by R-type thermocouple.

consistent. Regardless of heating and cooling rates, the sample was heated up to 1200 °C and kept at that temperature for 60 seconds before cooling. Cycle (i) is to remove the effect of the as-received microstructure, which is described as a “reset” of the microstructure. Cycle (ii) is a 5 K/s heating and cooling cycle that creates a benchmark for comparisons. Cycle (iii) was heated at 50 K/s and cycle (v) was heated at 0.17 K/s with previous cycle cooled at 5 K/s. Cycle (iv) was heated at 5 K/s with previously cooled at 50 K/s. Cycle (vi) was heated at 50 K/s with previously cooled at 0.17 K/s. Resistivity profiles and microstructures of Waspaloy from experiments described in Table IV are shown in Figures 8 through 11.

Figure 8 shows a plot of resistivity vs temperature for Waspaloy during three different rates (0.17, 5, and 50 K/s) of cooling from 1200 °C. In the supersolvus regime, resistivity decreases linearly as was observed for the heating curve in Figure 6(a). An instantaneous increase of resistivity indicates re-precipitation of γ' phase. Re-precipitation peaks in Figure 8 clearly show that faster cooling rate delays the γ' precipitation onset as summarized in Figure 7(a). During cooling, only the slowest cooling condition at 0.17 K/s gives two upward peaks as shown in Figure 8. The transition at 656 °C and the small peak at 563 °C are indications of possible nano-scale tertiary γ' precipitate nucleation and those temperatures agrees well with the 2nd burst of γ'

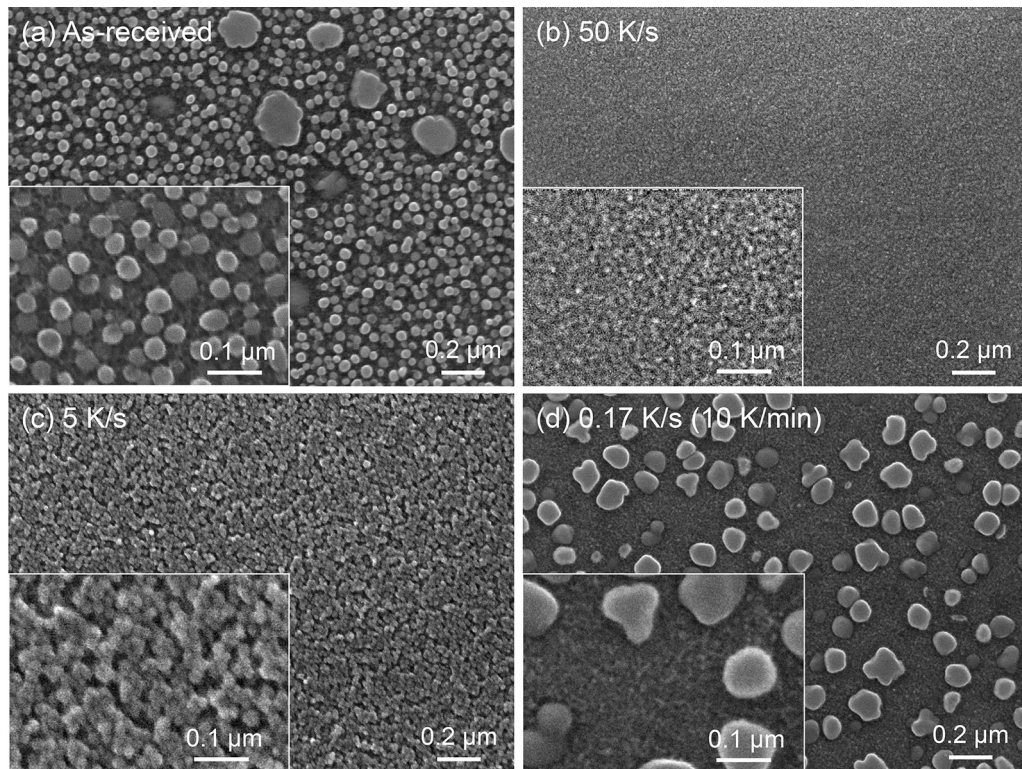


Fig. 9—Precipitate scale microstructure of Waspaloy after cooling from 1200 °C with different cooling rates using the ETMT. (a) As-received material with standard three step aging treatments. (b) Cooling rate at 50 K/s. (c) Cooling rate at 5 K/s. (d) Cooling rate at 0.17 K/s (10 K/min).

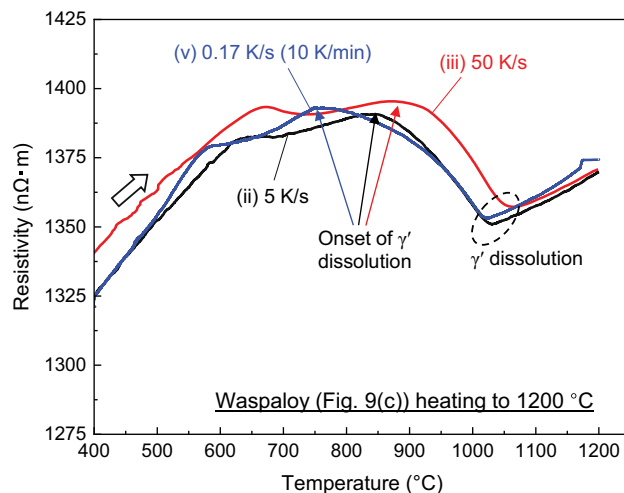


Fig. 10—Resistivity of Waspaloy during heating up to 1200 °C at different heating rates, 50, 5, and 0.17 K/s. The material was previously cooled down from 1200 °C at 5 K/s (microstructure shown in Fig. 8(c)). Temperature was measured by R-type thermocouple (Color figure online).

nucleation in slow cooled Rene88DT.^[54] Another study on a powder metallurgy alloy reported that tertiary precipitates can nucleate when the cooling rate is lower than 3 K/s.^[55] On the other hand, at faster cooling rates 5 and 50 K/s, such a peak was absent thus suggesting a monomodal precipitate size distribution.

To confirm the interpretation of the resistivity responses during cooling from 1200 °C at different cooling rates, the microstructure of Waspaloy, both as-received and following different thermal histories, were examined using the SEM (Figure 9). 50 K/s (Figure 9(b)) and 5 K/s (Figure 9(c)) have monomodal precipitate size distributions as suggested by resistivity plots in Figure 8. At a cooling rate of 0.17 K/s in Figure 9(d), there are seen to be both large secondary and very fine precipitates in the matrix, which agrees with an inflection interpreted as very fine γ' formation in Figure 8. Such very fine precipitates in Figures 9(b) and (d) are not clearly visible in the SEM. This is believed to be because etching removed the γ matrix to expose γ' precipitates and the very fine precipitates could not be easily retained when the matrix was removed.

The effect of the heating rate on Waspaloy after it had been cooled down at 5 K/s (Figure 9(c)) was compared and the results are shown in the resistivity-temperature plots of Figure 10. Regardless of heating rate, two upward peaks are apparent in Figure 10. All the peaks, including the γ' phase dissolution, are shifted toward higher temperature as the heating rate increases. All three heating rates indicate a lower temperature peak at 578 °C (0.17 K/s), 639 °C (5 K/s) and 671 °C (50 K/s). These lower temperature peaks are suggesting possible γ' precipitate reactions such as nucleation/dissolution/coalescence of the very fine scale ones during all the heating rates investigated.

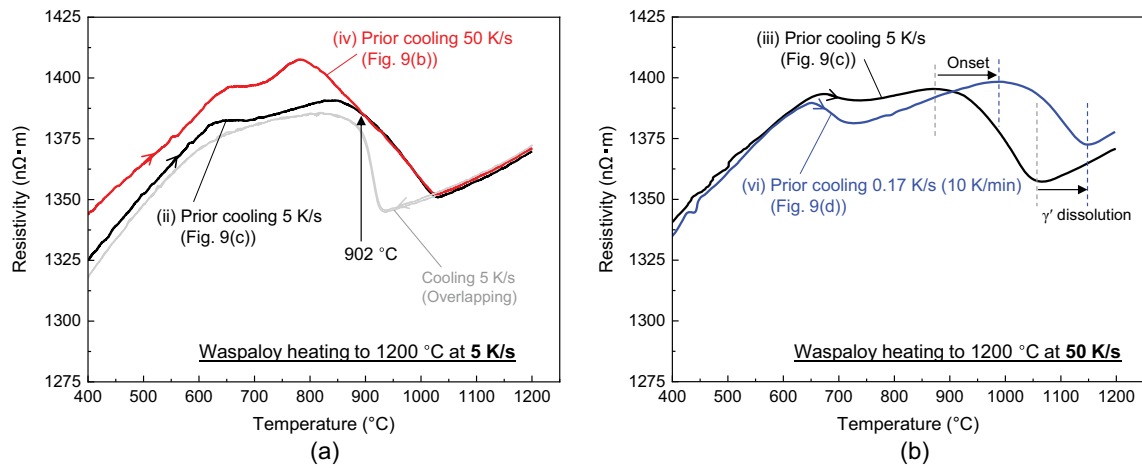


Fig. 11—Resistivity of Waspaloy with different initial microstructure during heating up to 1200 °C. Heating rates at 5 K/s (a) and 50 K/s (b). Temperature was measured by R-type thermocouple (Color figure online).

Using microstructures obtained by different cooling rates (Figure 9), the effect of precipitate sizes on resistivity-temperature plots was compared at a fixed heating rate, 5 K/s (Figure 11(a)). Prior cooling at 50 K/s resulted in a higher resistivity during heating compared to prior cooling at 5 K/s up to 902 °C. The number density of γ' precipitates is expected to be higher when the material has been previously cooled with a very rapid rate (Figures 9(b) vs (c)),^[56] and this potentially created nano-scale γ' precipitates that become a source of large electrical resistance.^[24,25] The major γ' dissolution (second peak at 780 °C) started at a lower temperature with higher resistivity for the material cooled at 50 K/s. Similar precipitation reactions were previously observed in an additively manufactured Ni-based superalloy without γ' phase and in supersaturated state.^[57] Because of substantially high number density of very fine γ' precipitates, Ostwald ripening was probably very active at the second peak that decrease of resistivity started earlier by combination of decreasing precipitate number density and γ' volume fraction. The complete dissolution temperature was, however, the same for the two different thermal histories because the heating rate was not fast enough that their microstructure became identical at 902 °C before the complete γ' dissolution. Moreover, the two cooling curves in Figure 11(a) are completely overlapping, which proves that the microstructure has been fully solutionized at 1200 °C and that an identical microstructure was obtained during cooling regardless of prior thermal history. This validates the assumption that 5 K/s can “reset” the Waspaloy microstructure regardless of its previous state.

A similar comparison was made using prior cooling rates at 5 and 0.17 K/s and the subsequent heating rate was fixed at 50 K/s (Figure 11(b)). Resistivity-temperature plots were initially the same and then started deviating at approximately 630 °C. The significant difference appeared in the major γ' dissolution, both onset and completion of γ' dissolution shifted to higher temperature for coarser microstructure. It is predicted

that a 0.17 K/s cooling created a coarser microstructure with a larger fraction of the γ' phase compared to cooling at 5 K/s and that resulted in a much higher dissolution temperature as longer time is expected for phase transformation to take place.

IV. APPLICATION OF *IN-SITU* RESISTIVITY MEASUREMENTS FOR CASE SPECIFIC STUDIES

Resistivity measurements were utilized for monitoring microstructure behavior during different types of case specific experiments and the results are reported in this section. The first one is on Waspaloy; it demonstrates an *in-situ* detection of γ' re-precipitation during heating cycles of the type seen in multi-pass welding. To rationalize the effect of dislocations and microstructure evolution on resistivity, two other case specific experiments were designed and performed on Ni-based SX superalloys, STAL15 and CMSX-4®. Experimental strategies, main results, and discussions regarding interpretation of resistivity responses are presented in this section.

A. Multi-pass Welding Simulation of Waspaloy

Welding is an important refurbishment technology for high temperature turbine applications, where casings, seals, blades, and other components' life can be effectively extended.^[58–60] The industrial challenge here is associated with defects, such as strain-age cracking, ductility exhaustion, and creation of a residual stress field, induced by precipitate evolution.^[58] Therefore, to best inform processing and appropriate control of microstructure, the precipitation evolution during thermal cycling must be better understood. For industrial relevance, a heating and cooling rate in the order of 100 K/s in between the last ageing temperature and near solidus point,^[61] *i.e.*, approximately 700 °C to 1200 °C was employed. Such experimentation is rarely done because the thermal cycling rate is normally beyond the

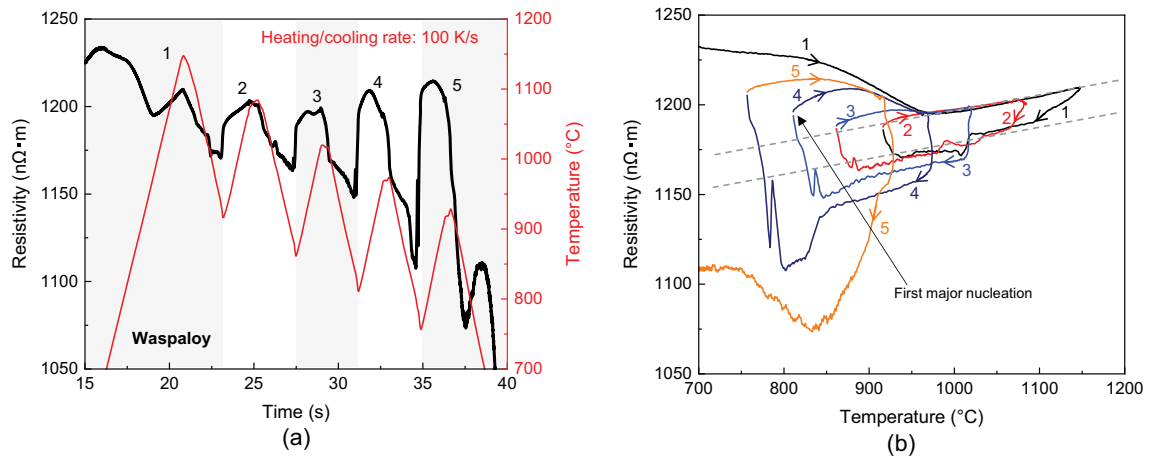


Fig. 12—(a) Resistivity (black) and temperature (red) during heating cycles on Waspaloy mimicking multi-pass welding. (b) Same resistivity was shown as a function of temperature. Dotted lines in (b) shows linear part that indicates resistivity behavior of solid solution. Temperature was measured by R-type thermocouple (Color figure online).

capability of a conventional resistance furnace, and *in-situ* monitoring of hardening precipitates (γ' or γ'') typically relies upon sufficient time for data collection during synchrotron radiation experiments.^[10,12,16]

Having the above in mind, we utilized the ETMT system to gain insight into the aforementioned scenario, where both *in-situ* monitoring of phase transition and high thermal cycling rates can be achieved. Waspaloy, a γ' strengthened weldable superalloy, was taken as an example to study the multi-pass welding in the solid state. The material was heated and cooled at 100 K/s with target temperatures in following order: 1150 °C → 925 °C (cycle 1) → 1075 °C → 875 °C (cycle 2) → 1025 °C → 825 °C (cycle 3) → 975 °C → 775 °C (cycle 4) → 925 °C → 725 °C (cycle 5) → RT. This temperature profile was intended to mimic heating during multi-pass welding of the material, similar to the Gleeble testing system that uses DC heating method. Resistivity and temperature vs time plots from this simulated multi-pass welding trial are shown in Figure 12.

Cycles 1 to 3 show similar resistivity peak where temperature is ranging between 875 °C and 1150 °C. The resistivity peak increased after the 4th cycle, which had a heating sequence from 825 °C to 975 °C. Since cycles 1 and 2 were above the re-precipitation temperature of this material, γ' precipitates are unlikely to be present in this material after the 2nd cycle. Nucleation temperature during cooling is at 870 °C according to the resistivity-time plot of the cooling cycle at 50 K/s in Figure 8. Therefore, limited precipitate nucleation is expected in the 2nd cycle as the material was cooled more rapidly at 100 K/s. Waspaloy was then heated up to 1025 °C during the 3rd cycle, which is very close to the solvus and minor nuclei can dissolve again. Dotted lines in Figure 12(b) are indicating linear resistivity that represents solid solution during the heating and the cooling. A significant increase in resistivity from this linear solid solution response was observed between end of the 3rd cycle from 834 °C to the beginning of 4th cycle up to 878 °C (see Figure 12(b)) meaning that

precipitates were allowed to nucleate and grow as the material was at a sufficiently high temperature for microstructure evolution. Resistivity again decreases during heating of 4th cycle as γ' dissolution starts again and reaches to the same level as the 3rd cycle. However, in another test with the same heating cycles, resistivity at 975 °C (maximum temperature for 4th cycle) was higher than the 3rd cycle at the same temperature. This suggests that the dissolution was not completed because 975 °C is below γ' solvus. Considering the previous study on the overheating effect,^[34,62] mechanical properties should be significantly different if the alloy after 3rd, 4th, and 5th cycles are compared because the *in-situ* resistivity measurement suggests that they have different γ' precipitate sizes and/or volume fraction.

B. Recrystallization of Pre-strained SX Superalloy

The next case study focuses on how resistivity measurements can be used in a rejuvenation study. Rejuvenation treatment is a repair method used for restoring the microstructure of cast superalloys after long thermal exposure that coarsens their microstructure.^[59] This method first applies re-solution treatment to dissolve γ' precipitates for stress relaxation and dislocation annihilation. Then, a standard aging treatment was applied to restore optimal microstructure. Creep properties of Ni-based SX superalloy can be extended by this method.^[63,64]

For this rejuvenation study, the temperature 950 °C was selected since deformation type at this temperature can trigger recrystallization at a relatively low strain magnitude.^[29,65,66] After the tensile pre-straining shown in Figure 5(b), the same material was heated using the ETMT with the following rejuvenation treatment; 5 K/s to 1100 °C → 1 K/s to 1225 °C → 30 minutes dwell at 1225 °C → 5 K/s to 1100 °C → 6 hours dwell at 1100 °C → 5 K/s to 100 °C. The rejuvenation temperature was chosen based on the DSC data (Figure 6(c)). The microstructure of the STAL15 sample after pre-straining and rejuvenation heat treatment was

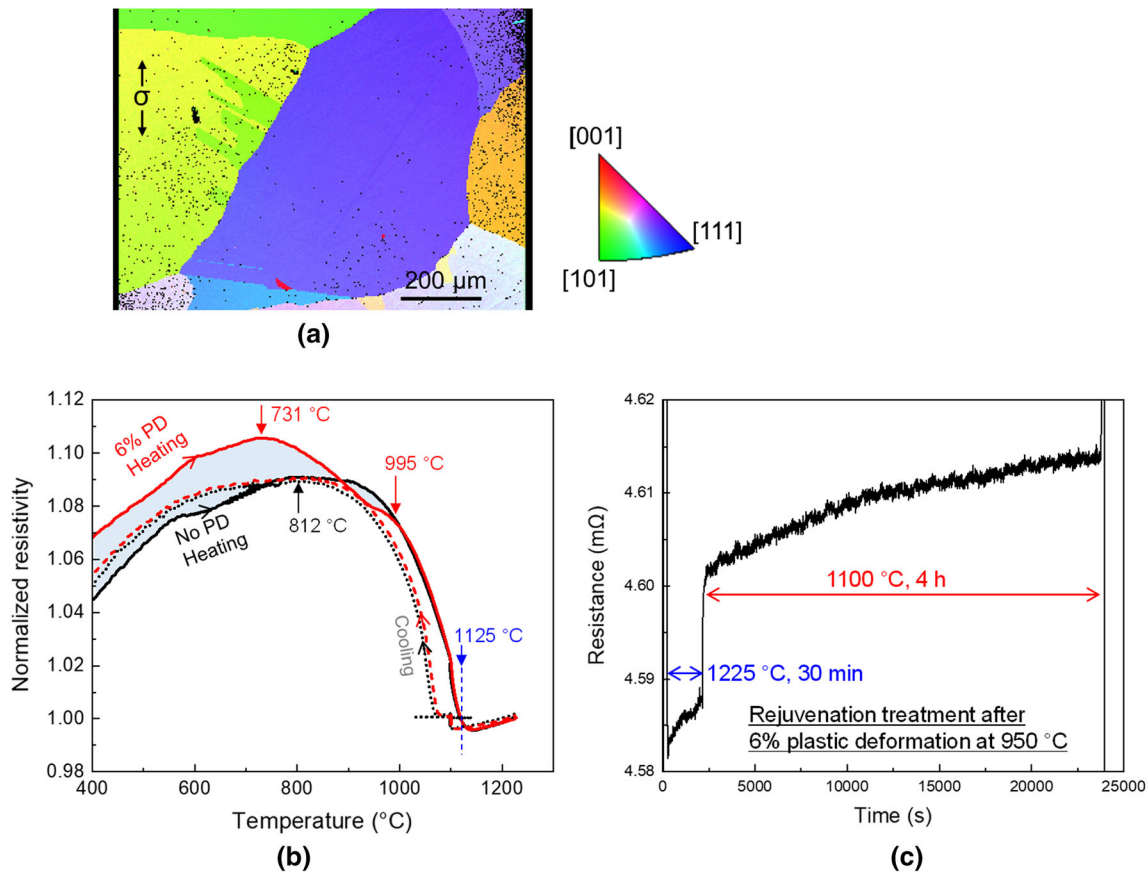


Fig. 13—Results on rejuvenation heat treatments performed on STAL15 using the ETMT system. (a) EBSD inverse pole figure referring to the loading direction after rejuvenation treatment. (b) Normalized resistivity of STAL15 during rejuvenation treatment, without plastic deformation (black) and with 6 pct plastic deformation (PD) at 950 °C (red). Resistivity was normalized using value when temperature reached 1225 °C. Solid and dotted curves are showing heating and cooling sequence, respectively. (c) Electrical resistance of pre-strained STAL15 during rejuvenation heat treatment consists of supersolvus re-solutioning at 1225 °C for 30 min and aging treatment at 1100 °C for 6 h (Color figure online).

analyzed using EBSD and recrystallization was observed throughout the sample cross section (Figure 13(a)). Clearly, the dislocation density developed during 6 pct tensile deformation was high enough to trigger the recrystallization during the re-solution heating up to 1225 °C. To identify the occurrence of recrystallization, the same straining was performed again on STAL15, but heating was up to 1125 °C this time. This sample also had recrystallized grains, which confirms that recrystallization occurred during heating sequence.

For the direct comparison, STAL15 alloy without pre-strain was also heated in the same procedures. Normalized resistivity curves of these two samples during heating, dwell, and cooling are shown in Figure 13(b). The resistivity was normalized using the value at 1225 °C where complete γ' dissolution and stress relaxation are expected. The dotted part of the resistivity curves in Figure 13(b) shows the profile after the re-solution treatment at 1225 °C. Two materials without/with plastic deformation have identical resistivity curves during the cooling down phase. During the heating sequence, a large deviation between the two materials is observed up to 995 °C (colored area in

Figure 13(b)), and pre-strained material shows different distinctive transition peaks as pointed by arrows. Details of resistivity change during dwells at 1225 °C and 1100 °C are shown in Figure 13(c). The electrical resistance at 1225 °C and at 1100 °C have shown increments during the entire period regardless of pre-strain. Since the material was fully (or at least mostly) solutioned at 1225 °C, increasing resistance at 1100 °C is referring to γ' precipitation and growth.

From resistivity profiles in Figure 13(b), and the fact that recrystallization was triggered during the heating sequence, the difference in normalized resistivity in Figure 13(b) is probably caused by the dislocations introduced during pre-straining. The normalized resistivity of the two materials (without/with pre-strain) followed the same profile after 1000 °C until the onset of cooling because the recrystallization eliminated dislocations during the heating phase. In summary, this type of experimental design^[33] has considerable potential as it will help to identify occurrence of recrystallization (during heating or dwell) for future studies on recrystallization of single crystal superalloys.

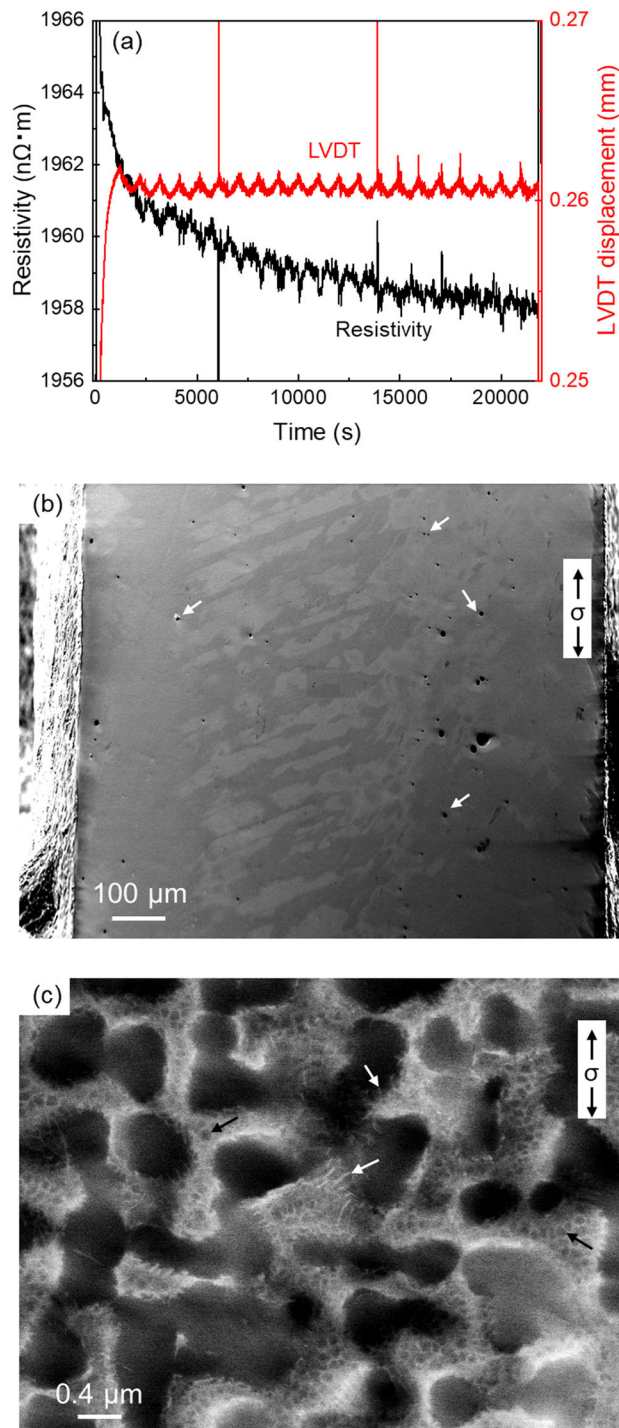


Fig. 14—Results of heat treatment applied to CMSX-4® after introducing 7 pct tensile plastic deformation at RT with strain rate of $3 \times 10^{-3} \text{ s}^{-1}$. (a) Resistivity and LVDT displacement during the heat treatment at 1100 °C for 6 h. (b) SEM image of sample after RT plastic deformation and heat treatment at 1100 °C for 6 h. White arrows are pointing at pores. (c) ECCI of the same sample in (b). White and black arrows are pointing at γ/γ' interfacial dislocations and tertiary γ' precipitates in the γ matrix, respectively.

C. Dislocation Network and Microstructure Evolution Induced by Pre-straining

The development of a γ/γ' dislocation network and evolution of the microstructure is well-established behavior during high temperature aging of Ni-based SX superalloys. Here we investigate the effect of pre-straining-induced microstructure evolution. This concept is taken from pre-straining studies on Ni-based SX superalloys that showed elastic strain around slip bands that accelerates the development of a γ/γ' interfacial dislocation network and γ' precipitate coarsening.^[65,67–69] Tensile deformation was performed on CMSX-4® at room-temperature (RT) using the ETMT system and interrupted at 7 pct plastic strain. The same CMSX-4® sample was then heat-treated at 1100 °C for 6 hours by DC current in the ETMT to develop a dislocation network and coarsen precipitates.

The change in electrical resistivity with time during heat treatment at 1100 °C for 6 hours after the tensile plastic deformation at RT is shown in Figure 14(a) along with the displacement measured by the LVDT. The decreasing resistivity is most probably due to the decreasing volume fraction of γ' phase. This material was previously heat-treated at 870 °C in the as-received state to optimize the γ' volume fraction (65 to 70 pct). The equilibrium volume fraction at 1100 °C is lower at ~ 50 pct.^[10,23,29,70] The increasing LVDT displacement indicates that the whole system, including the sample and water-cooled grips, needs approximately 1000 seconds to stabilize; however, it did not affect the result. If the displacement affects the resistivity, it should increase due to an elongation of measurement length, which was not the case for this experiment.

Figure 14(b) is a low magnification microstructure after the heat treatment at 1100 °C for 6 hours on the pre-strained sample. It is significant that a large number of pores are seen at the interdendritic area as pointed by arrows. According to a previous study, pores can nucleate and grow during microstructure evolution associated with dislocation climb.^[69] After the heat treatment, and as expected from the experiment design, a high density of γ/γ' interfacial dislocation networks (white arrows), coarsened γ' precipitates, and tertiary γ' precipitates within γ matrix (black arrows) are visible in the ECCI image of this sample (see Figure 14(c)).^[65] These features are all in accordance with previous studies on pre-strain effect on Ni-based SX superalloys.^[65,69]

Microstructure observation revealed following changes after the heat treatment at 1100 °C: increase of dislocation density; increase of precipitate number density; pores that nucleated and grew during dislocation development. From the fundamental results on Waspaloy, presented in a previous section, the distribution of finer γ precipitates strongly affects the resistivity of the material. Although Figure 14(c) reveals a large amount of fine tertiary γ' precipitates, these formed

during cooling from the experimental temperature and so did not affect the *in-situ* resistivity measurement at 1100 °C. Because metallurgical defects such as dislocations and pores become source of electrical resistance, they can increase resistivity during heat treatment. On the other hand, only the decreasing γ' volume fraction from 70 to 50 pct should decrease electrical resistivity in this experiment. Because resistivity continuously decreased as shown in Figure 14(a), it can be concluded that decreasing volume fraction of γ' precipitates at 1100 °C is the most responsible factor determines resistivity response.

V. DISCUSSION

Different factors that influence electrical resistivity of Ni-based superalloys are introduced in the different experiments conducted throughout the study. Consequently, different resistivity responses were observed in both the fundamental resistivity measurement and the case specific studies. In this section, the contribution of those factors is compared using results obtained and analyses from other studies. In addition, the benefits of *in-situ* monitoring of microstructure transitions by electrical resistivity are discussed.

A. Relationship Between Microstructure Transition and Resistivity

First, when the resistivity of commercially pure Ni in Figure 4 and that of superalloys in Figure 6 are compared, pure Ni has a significantly lower resistivity than the resistivity of alloys after complete dissolution of the γ' phase. It is widely known that solid solution of alloying element decreases electrical conductivity, in another words, it increases resistivity of metallic alloys. On the other hand, the effect of alloy composition was difficult to determine from limited results. Because resistivity of fully solutioned FCC has linear temperature-resistivity relationship like pure Ni, extrapolated resistivity can be used to compare different alloys. Extrapolated resistivity of Waspaloy, AD730®, STAL15, and CMSX-4® at 1300 °C in Figure 6 will be 1470, 1505, 1421, and 1440 nΩ m, respectively. These numbers suggest that the resistivity of Ni-based superalloys increases with grain boundaries (PX superalloys) or with higher alloying element fraction (AD730® for PX and CMSX-4® for SX). This seems consistent with the fact that grain boundaries can increase the resistivity of metallic alloys.^[29] However, notable resistivity difference was not found between recrystallized and non-recrystallized STAL15 in our case study. In addition, repeated heating of PX superalloys did not change resistivity at super solvus temperatures as shown in Figures 8, 10, and 11 although grain growth was observed in a sample after multiple heating cycles. In fact, grain boundary effect appears only if a grain size is below 100 nm,^[22] which is by far smaller than grain size of PX superalloys used in this study. Therefore, compositional effects of all alloys can be directly compared

using extrapolated resistivity at 1300 °C, which does not show a clear relationship between the alloy composition and the resistivity. It can be concluded that effects of both grain size and alloy composition of solid solution γ phase on the electrical resistivity are not a significant factor.

The precipitate size distribution and number density of precipitates need to be considered as revealed in Figures 8, 10, and 11. Resistivity was originally thought to be a simple function of γ' volume fraction, and this is true for high volume fraction SX superalloy like CMSX-4® after precipitate aging (typically between 1100 °C and 1150 °C) and stabilization aging (around 870 °C).^[23] However, a multi-modal precipitate size distribution will change the resistivity response during heating and cooling.^[24,25] The results show a decrease of resistivity at temperature lower than onset of main γ' dissolution when a nano-scale γ' precipitate dissolves (Figure 11(a)). This suggests that not only the volume fraction of ordered L1₂ phase, but also the area density of semi-coherent γ/γ' interfaces is a source of electrical resistance.

The γ/γ' interface being a resistivity source leads to another hypothesis that the magnitude of γ/γ' lattice misfit can influence the resistivity. Both CMSX-4® and STAL15 have the highest resistivity at around 850 °C in Figure 6; moreover, CMSX-4® has a much higher value. Lattice misfit of these alloys between 800 °C and 900 °C are similar (-0.1 pct) according to the literature (also lattice parameters of both γ and γ' phases are similar).^[11,41] On the other hand, CMSX-4® has a higher γ' volume fraction of 70 pct compared to that of STAL15 (60 pct) at the same temperature range.^[41,47,71] Therefore, the area density of γ/γ' interfaces which electrical current passes through is a factor that affects the resistivity of Ni-based superalloys, and the effect of γ/γ' misfit is negligible. Overall, the γ' volume fraction is the dominating factor as CMSX-4® has the highest resistivity of all four materials (according to ThermoCalc using the TTNi8 database, γ' volume fraction for AD730® and Waspaloy at 750 °C is 40 and 25 pct, respectively). Within the same material, the number density of γ' precipitates has a larger effect on the material's resistivity. The details of this size distribution effect need to be carefully analyzed in future using precipitation kinetics and diffusion models.^[25,72]

While different generations of precipitates are responsible for change of resistivity during continuous heating and cooling, and it can be analyzed in wide range of heating and cooling rates (0.1 to 100 K/s) in the ETMT system, attention must be paid to current inertia effect at the initiation of heating and end of cooling when the rate is relatively high (typically below 700 °C for 50 K/s and below 900 °C for 100 K/s). When electrical current is applied, depending on its intensity, temperature response has very small lag to the target temperature during initiation of heating. Also, when the material temperature is not following the programmed cooling rate, applied electrical current will be decreased drastically. These effects are especially apparent in Figure 8 where applied electrical current decreased rapidly after

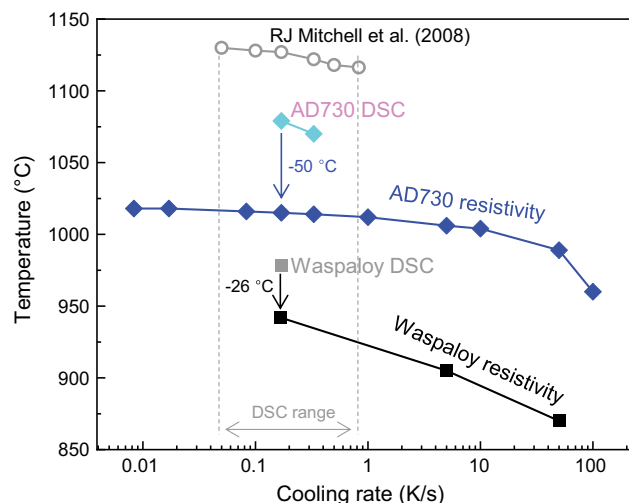


Fig. 15—Kinetics of γ' re-precipitate obtained by cooling of Waspaloy and AD730® from supersolvus temperature using DSC and the ETMT resistivity measurement. Data by RJ Mitchell *et al.* on experimental alloy UCI^[74] are also plotted for comparison of cooling rate range.

700 °C because the actual cooling rate could not follow programmed rate of 50 K/s, that leads to resistivity that is not representing microstructural response.

B. Re-precipitation During a Joule Heating

Contribution of other precipitates such as carbides and borides also needs to be considered. As explained using Figure 6, resistivity transition at $M_{23}C_6$ carbide was observed for alloys with carbon content, Waspaloy and AD730®. However, during cyclic heating experiments in Table IV, resistivity transition for carbide was not observed during any of heating and cooling. Possibility is that incoherent phases that preferably precipitate in grain boundary could not re-precipitate at the original location due to an electrical current effect as reported in the study by Nicolay *et al.*^[28] If minor phases that generally distributes in grain boundaries alternatively precipitated within a grain because of the current effect, their effect on resistivity can be smaller or similar to that of intragranular γ' precipitates but very low fraction that does not have much influence on overall resistivity value.

Indeed, γ' precipitates are the most important contributor of the resistivity. It has been shown many times that resistivity drastically increases with ordered $L1_2$ γ' phase precipitation. This is due to the effect of sublattice Al that increasing phonon vibration entropy of ordered $L1_2$ phase compared to that of disordered FCC phase.^[73] To understand more on the kinetics of γ' precipitation during cooling under the Joule heating, AD730® was repeatedly heated and cooled between 1000 °C and 1150 °C at different cooling rates ranging between 0.008 (0.5 K/min) and 100 K/s to define γ' re-precipitation temperatures. Results plotting γ' re-precipitation temperatures of Waspaloy and AD730® are shown in Figure 15. Re-precipitation temperatures of

Waspaloy and AD730® both showed difference between two methods, DSC and resistivity, that cannot be explained by the intrinsic error of temperature measurement using R-type thermocouple.^[45] AD730® seems to have re-precipitation temperature saturation at 1018 °C, which is by far lower than re-precipitation at 1079 °C detected by DSC or equilibrium temperature 1113 °C calculated by ThermoCalc. Although the difference is not as large as AD730®, this is the same for Waspaloy having lower re-precipitation temperature in the resistivity method. As summarized in Table III, difference between resistivity and DSC on γ' dissolution is within the range of the intrinsic error, and it is difficult to say that the electrical current accelerates dissolution kinetics or changes phase equilibrium. It seems that, only during the cooling, re-precipitation kinetics or phase equilibrium has been affected by the electrical current leading to a decreased γ' precipitation temperature.

C. Comparison of Different In-Situ Methods at High Temperature

As discussed, defining γ' precipitate dissolution or nucleation temperatures for different heating and cooling rates is clearly the advantage of *in-situ* resistivity measurement using the ETMT. For example, similar observations were made using synchrotron diffractometry even with a combination with mechanical test^[12,13]; however, the heating and cooling rate is usually limited to 0.5 to 10 K/s due to the heating method. On the other hand, resistivity can be used to find re-precipitation temperatures in very wide range of cooling rates as shown in Figure 15. This can also be extended to solvus vs re-precipitation relationship like Figure 7. Especially, faster heating/cooling rates are much more important considering rapid solidification and cooling in additive manufacturing, as-cast application, and solution heat treatment. Complex and faster temperature control capability was essential part of the case studies. Also, relatively small miniature sample and cost of the experiment can be considered as advantages in comparison to other methods. Indeed, as discussed in the previous subsection, re-precipitation mechanism seems to be affected by the electrical current and may not be representative of material's physical properties, which needs further study to understand the mechanisms.

In the current understanding, however, electrical resistivity measurement can be used to monitor microstructure only when the elastic/plastic deformations are absent since electrical potential measurement distance has a dominant effect (see Figure 5(b)). Combination of complex heating profiles with mechanical tests are specialty of the ETMT system.^[25,30,34,75–77] Because of the limitation, the resistivity could not yet ready for *in-situ* monitoring of superalloy's microstructural behavior during high temperature tests with relatively high deformation rate. Chance is that it can be used in low strain tests such as creep or stress relaxation tests where time dependent microstructure change is more important for understanding material properties and strain effect can be removed if strain is measured by non-contact video extensometry. Reliable

Table V. Comparison of Different High Temperature *In-Situ* Characterization Methods Used for Ni-Based Superalloys

	Resistivity in ETMT and Gleeble System	DSC	Synchrotron X-Ray, Neutron Diffraction	Transmission Electron Microscopy (TEM)
Speed	Up to 200 K/s	0.1 to 1 K/s	up to 10 K/s, requires time for sufficient intensity	requires time for data acquisition
γ/γ' Signal	very strong signal	by heat flux. Can be mixed with carbide. Signal becomes weaker at slower heating/cooling rate	separation post process is necessary	clearly visible but very local
Other Signals	weak, difficult to separate especially at slower rate	carbide, boride, different γ' size distributions can be detected	different crystal structures can be identified	elemental mapping by equipped EDS (energy dispersive X-ray spectroscopy)
γ' Volume Fraction	estimation is possible only if the material has monomodal γ' size distribution	requires modelling approach with careful data acquisition	relatively accurate Lattice misfit can be obtained as well	observation area is limited
Sample Size and Preparation	ETMT: 1×1 to 2×2 mm ² (40 mm length) Gleeble: 6 to 10 mm diameter	small piece 25 to 50 mg	depends on strength of beams	50 to 100 nm thickness, sample preparation is time consuming

deconvolution between (relatively large and rapid) plastic deformation and complex microstructural change is the challenge requiring further scholarly attention. Overall, depth of achievable information by resistivity is not at the level of other methods such as synchrotron diffractometry and high-resolution microscopy. Comparisons and trade-offs are summarized in Table V. Combination of different methods is indeed very useful for comprehensive *in-situ* characterization of materials.

VI. CONCLUSIONS

Electrical resistivity measurements were made during heating and cooling on commercially pure Ni and four different Ni-based superalloys (Waspaloy, AD730®, CMSX-4®, and STAL15) using an ETMT system that uses Joule heating for temperature control. Results are compared with the more conventional DSC approach to characterize the materials' resistivity response and some case studies utilizing *in-situ* resistivity measurement were presented. The following specific conclusions can be drawn:

1. Resistivity can be used to determine phase transition events such as dissolution and (re-)precipitation of phases (and Curie temperature) during heating and cooling of Ni-based superalloys. The phase transition behavior was compared with calculated equilibrium temperature and phases from ThermoCalc, and it showed consistency with DSC results during heating. On the other hand, γ' precipitation temperatures during continuous cooling using the ETMT were displaced from that observed by DSC, which suggests the effect of electrical current on changing precipitation mechanisms. One major advantage is detection of a phase transformation during rapid heating up to 100 K/s. This allows gaining fundamental understanding in phase transformations beyond the capacity of a conventional furnace arrangement (up to 1 K/s) which are limitations in calorimetry type techniques.
2. A wide range of heating/cooling rates (0.05 to 100 K/s) and different thermal histories were tested to evaluate dissolution and precipitation kinetics. Resistivity behavior during continuous heating/cooling provides information regarding microstructural change mainly related to γ' phase. However, sources of electrical resistance variation is rather complicated and they include crystal defects and secondary phases. The number density and volume fraction of γ' precipitates have the major influences on resistivity. The case study on pre-strained STAL15 showed that dislocation also affects the resistivity to some extent. Detailed study must be conducted in future to quantify their specific contributions.
3. Three different case studies are presented to demonstrate that *in-situ* resistivity measurement can

provide some indications of phenomena that occurred during thermal processing. Major re-precipitation was defined during simulated multi-pass welding on Waspaloy. Stress relaxation and recrystallization were suggested during rejuvenation of pre-strained Ni-based SX superalloy STAL15. Change of γ' volume fraction has been proven to have dominant effect on the resistivity during microstructural evolution and dislocation development of pre-strained CMSX-4®. Hence, it is shown that resistivity measurement in the Joule heating ETMT system can be utilized as a practical *in-situ* method for qualitative understanding of microstructural behavior during complex high temperature tests.

ACKNOWLEDGMENTS

The authors acknowledge financial support from the Hitachi Metals—University of Oxford UTC (University Technology Centre). Andrew Pearce (Instron) and T. Daniel Iskandar (Department of Materials, University of Oxford) are acknowledged for technical assistance in the experiments. The authors gratefully acknowledge Prof. D. Graham McCartney (Department of Materials, University of Oxford) for technical discussions and suggestions to improve quality of this manuscript. Dr. Magnus Hasselqvist (Siemens Industrial Turbomachinery), Zhe Chen (Siemens Energy), David Gustafsson (Siemens Energy), Dr. Jonathan Cormier (Institut Pprime), and Dr. Jérôme Blaizot (Aubert & Duval) are acknowledged for helping us to acquire experimental materials.

CONFLICT OF INTEREST

On behalf of all authors, the corresponding author states that there is no conflict of interest.

OPEN ACCESS

This article is licensed under a Creative Commons Attribution 4.0 International License, which permits use, sharing, adaptation, distribution and reproduction in any medium or format, as long as you give appropriate credit to the original author(s) and the source, provide a link to the Creative Commons licence, and indicate if changes were made. The images or other third party material in this article are included in the article's Creative Commons licence, unless indicated otherwise in a credit line to the material. If material is not included in the article's Creative Commons licence and your intended use is not permitted by statutory regulation or exceeds the permitted use, you will need to obtain permission directly from the copyright holder. To view a copy of this licence, visit <http://creativecommons.org/licenses/by/4.0/>.

REFERENCES

1. R.C. Reed: *The Superalloys: Fundamentals and Applications*, Cambridge University Press, Cambridge, 2006.
2. J.-Y. Guédou and L. Rémy: G. Cailletaud, J. Cormier, G. Eggeler, V. Maurel, and L.B.T.-N.B.S.C.A.L.S. Nazé, eds., Elsevier, 2022, pp. 3–19.
3. J. Cormier and C.-A. Gandin: G. Cailletaud, J. Cormier, G. Eggeler, V. Maurel, and L.B.T.-N.B.S.C.A.L.S. Nazé, eds., Elsevier, 2022, pp. 193–222.
4. M. Durand-Charre: *The Microstructure of Superalloys*, 1st ed. CRC Press, Boca Raton, 1997.
5. D.L. Sponseller: in *Superalloys 1996*, R.D. Kissinger, D.J. Deye, D.L. Anton, A.D. Cetel, M.V. Nathal, T.M. Pollock, and D.A. Woodford, eds., The Minerals, Metals, & Materials Society, 1996, pp. 259–70.
6. L.A. Chapman: *J. Mater. Sci.*, 2004, vol. 39, pp. 7229–36.
7. C.J. Burton: in *Superalloys*, 1976, pp. 147–57.
8. M.P. Jackson, M.J. Starink, and R.C. Reed: *Mater. Sci. Eng. A*, 1999, vol. 264, pp. 26–38.
9. H.T. Pang, N. D'Souza, H. Dong, H.J. Stone, and C.M.F. Rae: *Metall. Mater. Trans. A*, 2016, vol. 47A, pp. 889–906.
10. C. Schwalbe, A. Jacques, E. Galindo-Nava, C.N. Jones, C.M.F. Rae, and J. Cormier: *Mater. Sci. Eng. A*, 2019, vol. 740–741, pp. 182–86.
11. S. Huang, K. An, Y. Gao, and A. Suzuki: *Metall. Mater. Trans. A*, 2018, vol. 49A, pp. 740–51.
12. D.M. Collins, D.J. Crudden, E. Alabort, T. Connolley, and R.C. Reed: *Acta Mater.*, 2015, vol. 94, pp. 244–56.
13. J.-B. le Graverend, A. Jacques, J. Cormier, O. Ferry, T. Schenk, and J. Mendez: *Acta Mater.*, 2015, vol. 84, pp. 65–79.
14. G. Bruno and H.C. Pinto: *Mater. Sci. Technol.*, 2003, vol. 19, pp. 567–72.
15. A. Royer and P. Bastie: *Scr. Mater.*, 1997, vol. 36, pp. 1151–59.
16. F. Vogel, J. Cheng, S.B. Liang, C.B. Ke, S.S. Cao, X.P. Zhang, I. Zizak, A.M. Manzoni, J.M. Yu, N. Wanderka, and W. Li: *J. Alloys Compd.*, 2022, vol. 919, p. 165845.
17. S.L. Semiatin, S.-L. Kim, F. Zhang, and J.S. Tiley: *Metall. Mater. Trans. A*, 2015, vol. 46A, pp. 1715–30.
18. N. Chobaut, D. Carron, and J.M. Drezet: *Mater. Sci. Forum*, 2014, vol. 794–796, pp. 921–25.
19. D. Basak, R.A. Overfelt, and D. Wang: *Int. J. Thermophys.*, 2003, vol. 24, pp. 1721–33.
20. K.D. Maglič, N.L. Perović, and A.M. Stanimirović: *Int. J. Thermophys.*, 1994, vol. 15, pp. 741–55.
21. B. Noble and S.E. Bray: *Acta Mater.*, 1998, vol. 46, pp. 6163–71.
22. J.E. Darnbrough, B. Roebuck, and P.E.J. Flewitt: *J. Appl. Phys.*, 2015, vol. 118, p. 184302.
23. B. Roebuck, D. Cox, and R. Reed: *Scr. Mater.*, 2001, vol. 44, pp. 917–21.
24. I.-E. Benrabah, G. Altinkurt, M. Fèvre, M. Dehmas, B. Denand, F. Fossard, J.-S. Mérot, G. Geandier, D. Locq, and M. Perrut: *J. Alloys Compd.*, 2020, vol. 825, p. 154108.
25. N. D'Souza, M.C. Hardy, B. Roebuck, W. Li, G.D. West, and D.M. Collins: *Metall. Mater. Trans. A*, 2022, vol. 53A, pp. 2480–95.
26. H. Conrad: *Mater. Sci. Eng. A*, 2000, vol. 287, pp. 227–37.
27. D. Fabrègue, B. Mouawad, and C.R. Hutchinson: *Scr. Mater.*, 2014, vol. 92, pp. 3–6.
28. A. Nicolaï, J.M. Franchet, J. Cormier, R.E. Logé, G. Fiorucci, J. Fausty, M. Van Der Meer, and N. Bozzolo: *Metall. Mater. Trans. A*, 2021, vol. 52A, pp. 4572–96.
29. D.C. Cox, B. Roebuck, C.M.F. Rae, and R.C. Reed: *Mater. Sci. Technol.*, 2003, vol. 19, pp. 440–46.
30. N. D'Souza, B. Roebuck, D.M. Collins, G.D. West, and C. Panwisawas: *Mater. Sci. Eng. A*, 2020, vol. 773, p. 138862.
31. E. Madhi and P.B. Nagy: *AIP Conf. Proc.*, 2009, vol. 1096, pp. 1209–15.
32. R.J. White, G.A. Swallow, S.B. Fisher, and K.M. Miller: *J. Nucl. Mater.*, 1975, vol. 55, pp. 273–78.
33. S.J. Perry, N. D'Souza, D.M. Collins, B. Roebuck, and H.B. Dong: *Metall. Mater. Trans. A*, <https://doi.org/10.1007/s11661-022-06861-5>.
34. S. Utada, R. Sasaki, R.C. Reed, and Y.T. Tang: *Mater. Des.*, 2022, vol. 221, p. 110911.
35. G. Pottlacher, H. Hosaeus, E. Kaschnitz, and A. Seifert: *Scand. J. Metall.*, 2002, vol. 31, pp. 161–68.
36. B. Roebuck, D.C. Cox, and R.C. Reed: in *Superalloys 2004*, K.A. Green, T.M. Pollock, H. Harada, T.E. Howson, R.C. Reed, J.J. Schirra, and S. Walston, eds., The Minerals, Metals, & Materials Society, 2004, pp. 523–28.
37. C.T. Sims: in *Superalloys 1984*, 1984, pp. 399–419.
38. A. Kracke: in *7th International Symposium on Superalloys 718 and Derivatives*, E.A. Ott, J.R. Groh, A. Banik, I. Dempster, T.P. Gabb, R. Helmink, X. Liu, A. Mitchell, and G.P. Sjöberg, eds., The Minerals, Metals, & Materials Society, 2010, pp. 13–50.
39. A. Devaux, B. Picqué, M.F. Gervais, E. Georges, T. Poulain, and P. Héritier: *Superalloys 2012*, 2012.
40. A. Devaux, L. Berglin, L. Thebaud, R. Delattre, C. Crozet, and O. Nodin: *MATEC Web Conf.*, <https://doi.org/10.1051/mateconf/20141401004>.
41. A. Sato, J.J. Moverare, M. Hasselqvist, and R.C. Reed: *Metall. Mater. Trans. A*, 2012, vol. 43A, pp. 2302–15.
42. J.J. Moverare, M. Segersäll, A. Sato, S. Johansson, and R.C. Reed: *Superalloys 2012*, 2012.
43. K. Harris, G.L. Erickson, W.D. Brentnall, J.M. Aurrecoechea, S.L. Sikkenga, and K.G. Kubarych: in *Superalloys 1992*, S.D. Antolovich, R.W. Stursrud, R.A. MacKay, D.L. Anton, T. Khan, R.D. Kissinger, and D.L. Klarstrom, eds., 1992, pp. 297–306.
44. S.L. Semiatin, D.W. Mahaffey, N.C. Levkulich, and O.N. Senkov: *Metall. Mater. Trans. A*, 2017, vol. 48A, pp. 5357–67.
45. Y.T. Tang, C. Schwalbe, M. Futoma, B. Roebuck, S. Utada, and R.C. Reed: *Metall. Mater. Trans. A*, <https://doi.org/10.1007/s11661-022-06869-x>.
46. S. Sulzer, E. Alabort, A. Németh, B. Roebuck, and R. Reed: *Metall. Mater. Trans. A*, 2018, vol. 49A, pp. 4214–35.
47. A. Epishin, B. Fedelich, M. Finn, G. Künecke, B. Rehmer, G. Nolze, C. Leistner, N. Petrushin, and I. Svetlov: *Crystals*, 2021, vol. 11, p. 152.
48. R.E. Silber, R.A. Secco, and W. Yong: *J. Geophys. Res. Solid Earth*, 2017, vol. 122, pp. 5064–81.
49. H. Liu, L. Zheng, D. Wang, X. Wei, H. Min, Y. Jin, and Q. Tai: *J. Mater. Eng. Perform.* DOI:<https://doi.org/10.1007/s11665-022-06768-7>.
50. F. Masoumi, M. Jahazi, D. Shahriari, and J. Cormier: *J. Alloys Compd.*, 2016, vol. 658, pp. 981–95.
51. H.E. Collins: in *1st International Symposium on Structural Stability of Superalloys*, 1968, pp. 171–98.
52. S. Utada, Y. Joh, M. Osawa, T. Yokokawa, T. Sugiyama, T. Kobayashi, K. Kawagishi, S. Suzuki, and H. Harada: *Metall. Mater. Trans. A*, 2018, vol. 49A, pp. 4029–41.
53. C. Rae, M. Karunaratne, C. Small, R. Broomfield, C. Jones, and R. Reed: in *Superalloys 2000*, 2000, pp. 767–76.
54. A.R.P. Singh, S. Nag, S. Chattopadhyay, Y. Ren, J. Tiley, G.B. Viswanathan, H.L. Fraser, and R. Banerjee: *Acta Mater.*, 2013, vol. 61, pp. 280–93.
55. L. Zhu, H. Pan, J. Cheng, L. Xiao, J. Guo, and H. Ji: *J. Alloys Compd.*, 2022, vol. 918, p. 165677.
56. S.S. Babu, M.K. Miller, J.M. Vitek, and S.A. David: *Acta Mater.*, 2001, vol. 49, pp. 4149–60.
57. Y.T. Tang, C. Panwisawas, B.M. Jenkins, J. Liu, Z. Shen, E. Salvati, Y. Gong, J.N. Ghoussoub, S. Michalik, B. Roebuck, P.A.J. Bagot, S. Lozano-Perez, C.R.M. Grovenor, M.P. Moody, A.M. Korsunsky, D.M. Collins, and R.C. Reed: *Addit. Manuf.*, 2022, p. preprint.
58. M.B. Henderson, D. Arrell, R. Larsson, M. Heobel, and G. Marchant: *Sci. Technol. Weld. Join.*, 2004, vol. 9, pp. 13–21.
59. F. Pedraza and S. Utada: in *Nickel Base Single Crystals Across Length Scales*, G. Cailletaud, J. Cormier, G. Eggeler, and V. Maurel, eds., Elsevier, 2022, pp. 259–81.
60. M. Gäumann, C. Bezençon, P. Canalis, and W. Kurz: *Acta Mater.*, 2001, vol. 49, pp. 1051–62.
61. R.C. Reed and H.K.D.H. Bhadeshia: *Acta Metall. Mater.*, 1994, vol. 42, pp. 3663–78.
62. J. Andersson, G.P. Sjöberg, L. Viskari, and M. Chaturvedi: *Mater. Sci. Technol.*, 2013, vol. 29, pp. 43–53.
63. B. Rutter, D. Bürger, L.M. Roncery, A.B. Parsa, P. Wollgramm, G. Eggeler, and W. Theisen: *Mater. Des.*, 2017, vol. 134, pp. 418–25.

64. O.M. Horst, B. Rutttert, D. Bürger, L. Heep, H. Wang, A. Dlouhý, W. Theisen, and G. Eggeler: *Mater. Sci. Eng. A*, 2019, vol. 758, pp. 202–14.
65. S. Utada, J. Rame, S. Hamadi, J. Delautre, L. Mataveli Suave, P. Villechaise, and J. Cormier: in *Superalloys 2020*, S. Tin, M. Hardy, J. Clews, J. Cormier, Q. Feng, J. Marcin, C. O'Brien, and A. Suzuki, eds., Springer International Publishing, 2020, pp. 240–52.
66. Z. Li, X. Fan, Q. Xu, and B. Liu: *Mater. Lett.*, 2015, vol. 160, pp. 318–22.
67. M. Sakaguchi, M. Ike, and M. Okazaki: *Mater. Sci. Eng. A*, 2012, vol. 534, pp. 253–59.
68. S. Hamadi, F. Hamon, J. Delautre, J. Cormier, P. Villechaise, S. Utada, P. Kontis, and N. Bozzolo: *Metall. Mater. Trans. A*, 2018, vol. 49A, pp. 4246–61.
69. S. Utada, J. Rame, S. Hamadi, J. Delautre, P. Villechaise, and J. Cormier: *Mater. Sci. Eng. A*, 2020, vol. 789, p. 139571.
70. S. Utada, L. Després, and J. Cormier: *Metals*, 2021, vol. 11, p. 1610.
71. R.C. Reed, D.C. Cox, and C.M.F. Rae: *Mater. Sci. Eng. A*, 2007, vol. 448, pp. 88–96.
72. A. Deschamps and C.R. Hutchinson: *Acta Mater.*, 2021, vol. 220, p. 117338.
73. B. Fultz, L. Anthony, L.J. Nagel, R.M. Nicklow, and S. Spooner: *Phys. Rev. B*, 1995, vol. 52, pp. 3315–21.
74. R.J. Mitchell, M. Preuss, S. Tin, and M.C. Hardy: *Mater. Sci. Eng. A*, 2008, vol. 473, pp. 158–65.
75. S. Sulzer, Z. Li, S. Zaefferer, S.M. Hafez Haghighat, A. Wilkinson, D. Raabe, and R. Reed: *Acta Mater.*, 2020, vol. 185, pp. 13–27.
76. Y.T. Tang, N. D'Souza, B. Roebuck, P. Karamched, C. Panwisawas, and D.M. Collins: *Acta Mater.*, 2021, vol. 203, p. 116468.
77. J.N. Ghoussoub, Y.T. Tang, W.J.B. Dick-Cleland, A.A.N. Németh, Y. Gong, D.G. McCartney, A.C.F. Cocks, and R.C. Reed: *Metall. Mater. Trans. A*, 2022, vol. 53A, pp. 962–83.

Publisher's Note Springer Nature remains neutral with regard to jurisdictional claims in published maps and institutional affiliations.